FISEVIER

Contents lists available at ScienceDirect

CIRP Journal of Manufacturing Science and Technology

journal homepage: www.elsevier.com/locate/cirpj



Full-length article

In-situ IR imaging for modeling energy transfer and its relationship to shear strength of the weld interface in ultrasonic additive manufacturing



Gowtham Venkatraman ^a, Umair Shah ^b, Xun Liu ^b, Marcelo J. Dapino ^{a,*}

- ^a NSF IUCRC Smart Vehicle Concepts Center, Department of Mechanical and Aerospace Engineering, The Ohio State University, 201 W 19th Ave., Columbus, OH 43210, USA
- ^b Edison Joining Technology Center, The Ohio State University, 1248 Arthur Adams Drive, Columbus, OH 43221, USA

ARTICLE INFO

Article history: Available online 14 April 2023

Keywords:
Ultrasonic additive manufacturing (UAM)
Advanced manufacturing technologies
Process modeling
In-situ thermal measurements
Infrared thermography

ABSTRACT

A framework to map the flow of energy is necessary for quantifying the relationship between process parameters and shear strength of the weld interface (weld strength) in ultrasonic additive manufacturing (UAM). In-situ infrared thermography measurements were used to validate transient thermal finite element (FE) models of heat transfer for the UAM of 6061- and 5052- series aluminum alloys. An analytical structural model was developed to estimate the stress distribution and heat input in the UAM process. The combined model is used to build an empirical energy-strength correlation that maps process parameters to the weld strength of UAM parts by identifying the driving energy (the energy of plastic deformation) for bond formation for Al-Al joining from the participating energies in UAM. Good agreement is found between model predictions and experimental weld strength measurements. The framework enables the definition of a figure of merit to quantify the portion of input energy from the welder that is used for bond formation.

© 2023 CIRP.

Introduction

Ultrasonic additive manufacturing (UAM) is a solid-state 3D printing process based on continuous ultrasonic metal welding, detailed in [29]. A rotating sonotrode presses metallic foilstock against a similar or dissimilar metallic base, which in conjunction with lateral ultrasonic vibrations serves to disperse oxides, plastically deform asperities, and generate metallurgical welding through intimate metal to metal contact. The process is used to print successive layers of thin metallic foil onto a baseplate. The welding tool is also integrated into a CNC machine which enables the integration of subtractive processes to create near net-shape parts. No detailed models exist to describe the relationship between process parameters, weld temperature, and weld strength in UAM. Such models are required to guide the development of process settings and minimize laborious trial and error welding.

Understanding the role of heat generation and weld temperature in the UAM process is critical to developing energy flow models for UAM. To that end, it is necessary to quantify the partition of the input energy into the energy of plastic deformation, which drives bond formation, and friction, which contributes to heat generation.

The UAM process has similarities to cold roll bonding (CRB), a solidstate joining process where two foils are rolled under high pressure to create a weld. In this study, UAM is treated as ultrasonically-assisted cold-roll bonding.

Fujii et al. [8] found that the high amplitude cyclic deformation applied by the UAM welder causes the oxide layer to crack. Mohamed and Washburn [16] proposed that the formation of a bond between the two metal foils in solid-state welding after asperities are crushed and flattened requires an activation energy. Work by [13] showed that UAM shows a similar threshold energy requirement for bond formation. Several studies have tried to develop an analytical expression for the relationship between deformation reduction R and the bond strength ratio (to the bulk strength) η in cold roll bonding. A simple model accounting for the threshold deformation R_{th} is found in the work of [30]:

$$\eta = H \left(1 - \frac{(1 - R)^2}{(1 - R_{th})^2} \right), \tag{1}$$

where *H* is an empirical hardening coefficient.

Certain models for bond strength in solid-state welding incorporate the extrusion of the metal through cracks in the oxide layer [5]. Such models do not necessarily apply to UAM because the cyclic stress loads from the ultrasonic vibrations in UAM have the effect of cracking and dispersing the oxide layer. This is supported by microstructural studies by [32] that found no oxide layers in bonded

^{*} Corresponding author.

E-mail address: dapino.1@osu.edu (M.J. Dapino).

regions of UAM samples. The superposition of stresses introduced by the out-of-plane ultrasonic vibrations in UAM is expected to reduce the deformation required for bonding. In this manuscript, the activation energy will be assumed to be proportional to the energy of plastic deformation as it was found by [16] that plastic deformation is a key requirement for solid-state welding.

A transient thermal finite element (FE) model is developed to predict the weld temperature as a function of heat energy generated. Zhang et al. [35] identified that the temperature increase plays a role in bond formation, though a key feature of the UAM process is the low formation temperature. Intermetallics often form in fusion processes with dissimilar metals because elevated temperatures permit mixing and diffusion. In contrast, melting and subsequent solidification are absent in UAM. Obielodan et al. [17] showed that this enables the joining of dissimilar metals without the formation of brittle intermetallic phases. Gunduz et al. [9] found that higher temperatures improve inter-diffusion and localized melting at the interface in the ultrasonic welding of aluminum and zinc. Siggard [23] identified that the low temperature aspect of the process enables the embedment of temperature-sensitive electronics in metal structures. Using thermocouples embedded at the weld interface, the work by [25] showed that the peak temperature reaches near 150°C for welding aluminum and copper alloys with a 9 kW welder. Infrared imaging has been used to calibrate simple 2-D models of ultrasonic welding processes in the work of [12].

Real-time temperature monitoring of the ultrasonic welding process was discussed by [4]. A 2-D finite element thermal model for UAM was developed by [31], and reported that the heat generation due to friction is twice the heat generation due to plastic deformation for AA1100 aluminum alloy, whereas [34] reported that all the energy lost during welding is due to friction. However, [25] proposed that heat generation due to plastic deformation is much higher than that from friction. Analytical expressions were used to estimate the heat generation and the 3-D temperature fields, which were compared against weld temperature measurements taken using thermocouples. Although thermocouples are a conventional means to measure weld temperature, they have some inherent disadvantages when compared to non-contact methods. Adding a thermocouple to a workpiece in a channel modifies the heat capacity of the surrounding region, and the measured temperature could be different from the temperatures reached if the thermocouple were not placed. The thermocouple also needs to be very sensitive with a high frequency bandwidth to accurately measure the very high heating rates of over 3000°C/s reported for ultrasonic welding by [6] and for ultrasonic additive manufacturing by [21]. In addition, thermocouples only provide a single-point measurement.

Non-contact infrared (IR) imaging has several advantages over thermocouples for temperature monitoring in UAM. IR cameras have detectors that absorb a narrow band of infrared radiation in the electromagnetic spectrum and transform it into a 2-dimensional temperature field. The wavelength emitted is given by Wein's displacement law, as described for instance by [19]. The main advantages of using IR cameras are their quick response time and high sensitivity. A high-resolution 2-dimensional grid of data points can be obtained which provides a more detailed thermal field data. IR imaging has been used to predict small welding defects with high resolving power in arc welding by [14] and laser welding by [24]. The estimated weld temperature can be used to estimate the heat generated in the UAM process in conjunction with a thermal finite element (FE) model.

Analytical model development

Fig. 1 shows the steps required to estimate the plastic deformation E_{pl} and the frictional dissipation energy E_f for UAM as a function of process parameters. A transient thermal FE model is developed

using COMSOL to estimate the temperature distribution T(x, y, z) in the workpiece and the heat input Q_{UAM} from the measured peak temperature T_{UAM} as detailed in Section 3. The temperature distribution is used to estimate the temperature-dependent properties such as yield strength of the workpiece to be used in the structural model. An LTI model of the weld assembly is used to estimate the shear force F_s from the process parameters as detailed in [11]. The structural model takes the weld force F_n and shear force F_s as inputs to estimate each of the energies E_{pl} and E_f .

Modeling assumptions

Developing a comprehensive coupled thermal-mechanical model for UAM requires the simulation of several thousand cycles of high-frequency 20 kHz vibrations, which is computationally expensive. Hence, an analytical framework is developed to approximate the stress, strain, and temperature fields in the UAM process. The thermal and structural problems are decoupled, and the weld temperature from the thermal FE model is used as input in the structural problem to determine the temperature-dependent yield strength, seen in Fig. 1. The heat energy generated is estimated from the structural model.

The following simplifying assumptions are made. First, it is assumed that the variation of the Z-direction normal stress from the welder-foil contact surface to the foil-foil contact surface is negligible since the thickness t_f of the foil (150 μ m) is significantly lower than its width w (25.4 mm). Second, the elongation in the rolling direction (X-direction) due to rolling is neglected, and X-direction stresses and strains are neglected. This leads to the overestimation of the energy of plastic deformation in soft materials like Al 6061-O where some elongation is observed in the weld foil after UAM. Third, the elastic component of the total strain is considered to be negligible compared to the plastic strain due to the large plastic deformations imparted by the welder (10–20 μ m).

Fourth, the von-Mises criterion is used as the yield criterion for the initiation of plasticity. Previous work by [22] on the mechanical behavior of 2024 aluminum alloys found that there was no strainrate dependence on plastic deformation up to strain rates of $5000 \, \mathrm{s}^{-1}$, which is close to the typical strain rate in UAM calculated from the maximum shear strain $\gamma = |\delta_{welder}|/t_f$ and the welder frequency of 20 kHz. Hence strain-rate dependence is not modeled, but this assumption can be modified for describing the UAM of different materials. The anisotropy in the material yield parameters is ignored for simplicity, but the rolled foil is expected to have some anisotropy between the rolled and transverse directions. Fifth, no slip is assumed between the welder and the top of the weld foil since the roughened welder surface, whose roughness was measured using a surface profilometer to be between 9 and 11 μ m R_a , will produce sufficient grip to prevent slipping.

Model for plastic deformation energy

Normal and shear stresses

If Hertzian contact was assumed, the normal stress $\sigma_{zz}^{Hz}(x)$ under the welder, the maximum normal stress P_{max}^{Hz} , and the contact halfwidth a^{Hz} would be given by

$$\sigma_{zz}^{Hz} = P_{max}^{Hz} \sqrt{1 - \left(\frac{x}{a^{Hz}}\right)^2} \tag{2}$$

$$P_{max}^{Hz} = \sqrt{\frac{W_d E^*}{\pi R}}, \quad \frac{1}{E^*} = \frac{1 - \gamma_{St}^2}{E_{St}} + \frac{1 - \gamma_{Al}^2}{E_{Al}}$$
 (3)

$$a^{Hz} = 2\sqrt{\frac{W_d R}{\pi E^*}} \tag{4}$$

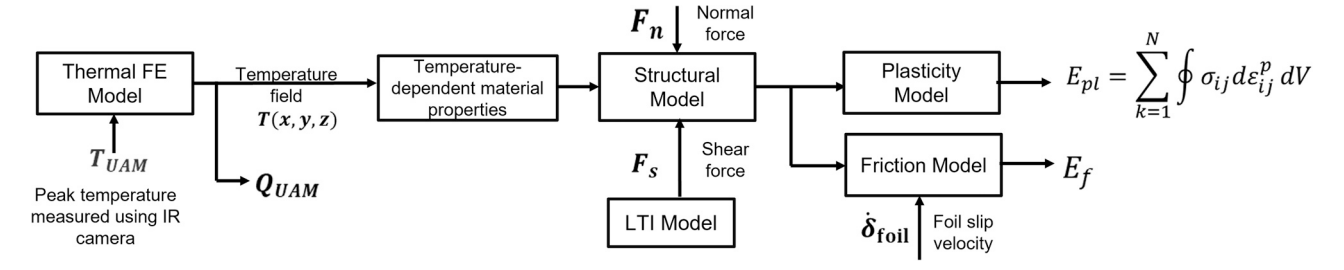


Fig. 1. Schematic of the thermal-structural model used to estimate the energy of plastic deformation E_{pl} and the energy dissipated due to friction E_{f} .

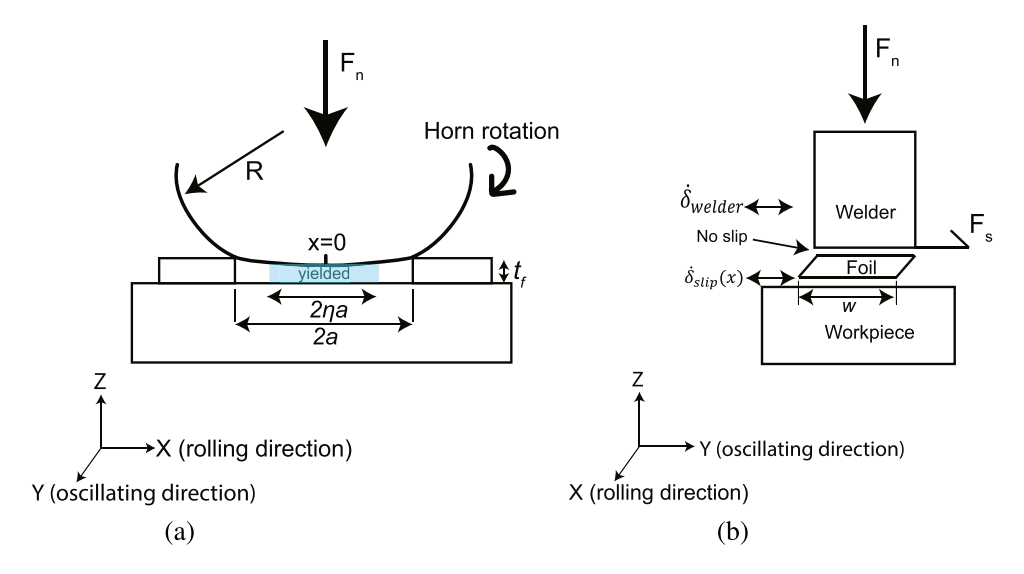


Fig. 2. Illustration of the forces and vibration velocities during UAM: (a) the contact width 2a of the weld foil of thickness t_f with the yielded foil material under the welder, where η is the fraction of the contact width where the foil has plastically yielded; (b) the top of the foil of width w sticks to the welder and the bottom of the foil has a slip velocity profile $\dot{c}_{slip}(x)$ with the workpiece (previously welded foil or baseplate). The vibration velocity of the workpiece is assumed to be small in comparison to the welder's vibration velocity.

where E^* is the effective modulus of the steel-aluminum interface calculated from the modulus, $W_d = F_n/w$ is the vertical weld force F_n per unit width w, and R is the radius of the steel welder as described by [2]. It is also noted by [2] that tangential forces have a insignificant effect on the shape and size of the contact area, allowing the stresses from the normal and tangential forces to be assumed to be independent of each other. Note that x = 0 is directly under the axis of rotation of the welder (Fig. 2).

For a steel welder on aluminum foil, the maximum stress for a 5000 N weld force would be 276 MPa, which is higher than the yield strength of even work-hardened foil materials such as Al 5052-H38 (yield strength = 255 MPa) and Al 6061-H18 (yield strength = 230 MPa). Thus, the key Hertzian assumption of elastic behavior is invalid, and the stress distributions obtained cannot be directly used. The model is extended to include the effect of the material yielding by proposing that after yielding, the contact half-width continues to increase to distribute the normal load over a larger load-bearing area until the forces are balanced. It is assumed that the normal load distribution in the plastic regime has a similar distribution as (2) with a new maximum normal stress P_{max} and contact half-width a, as shown in Fig. 2(a). The maximum normal stress is assumed to be the yield stress σ_y of the material. The new contact half-width a can be computed using the following expressions:

$$\sigma_{zz} = P_{max} \sqrt{1 - \left(\frac{x}{a}\right)^2},\tag{5}$$

$$F_n = \int_{-a}^{a} P_{max} \sqrt{1 - \left(\frac{x}{a}\right)^2} w dx = \frac{\pi P_{max}. \ a. \ w}{2}.$$
 (6)

$$\Rightarrow P_{max}. \ a. \ w = \frac{2F_n}{\pi}. \tag{7}$$

The shear force F_s applied by the welder results in a shear stress distribution $\tau_{Yz}(x)$ in the YZ-plane such that

$$\int_{-a}^{a} \tau_{yz}(x)wdx = F_{s}.$$
(8)

The terms $\sigma(x)$ and $\tau(x)$ will henceforth be used in place of $\sigma_{zz}(x)$ and $\tau_{yz}(x)$ respectively for brevity.

Yield criterion

The state of stress of a stress element taken at a location x with breadth dx can be represented using the Cauchy stress tensor σ_{ii}

$$\sigma_{ij} = \begin{bmatrix} 0 & 0 & 0 \\ 0 & 0 & \tau(x) \\ 0 & \tau(x) & -\sigma(x) \end{bmatrix}.$$
 (9)

The deviatoric stress is calculated as the difference of the stress tensor and one-third of its trace

$$s_{ij} = \begin{bmatrix} \frac{\sigma(x)}{3} & 0 & 0\\ 0 & \frac{\sigma(x)}{3} & \tau(x)\\ 0 & \tau(x) & -2\frac{\sigma(x)}{3} \end{bmatrix}.$$
 (10)

Classical J_2 flow theory is used to describe the yield behavior of the material, and the von-Mises criterion is used for the yield criterion. It is assumed that the material in the region – $\eta a < x < \eta a$ has plastically yielded as seen in Fig. 2(a), and thus meets the von-Mises yield criterion

G. Venkatraman, U. Shah, X. Liu et al.

$$J_2 = \frac{1}{2} s_{ij} s_{ij} = \sigma(x)^2 / 3 + \tau(x)^2 = \sigma_y^2 / 3 \text{for} - \eta a < x < \eta a, \tag{11}$$

where $\sigma_y = \sigma_y(T_{weld})$ is the temperature-dependent yield strength of the foil material at the weld temperature T_{weld} . Note that hardening effects are not included in this model for simplicity, which leads to an underestimation of the stress values. The expression (11) can be used to obtain the shear stress distribution from a given normal stress distribution from (5) as follows:

$$\tau(x) = \frac{1}{\sqrt{3}} \sqrt{\sigma_y^2 - P_{max}^2 \left(1 - \left(\frac{x}{a}\right)^2\right)}$$
(12)

Note that the shear stress will oscillate along with the shear force as a 20 kHz sine wave, but the peak value is used for simplicity. Neglecting shear stresses in the regions not yielded and substituting (12) in (8) and using a dummy variable $\alpha = \frac{x}{a}$ one obtains

$$F_{s} = \int_{-\eta a}^{\eta a} \frac{1}{\sqrt{3}} \sqrt{\sigma_{y}^{2} - P_{max}^{2} \left(1 - \left(\frac{x}{a}\right)^{2}\right)}. w. dx$$
 (13)

$$= \int_{\alpha=-\eta}^{\alpha=\eta} \frac{w. a}{\sqrt{3}} \sqrt{\sigma_y^2 - P_{max}^2 (1-\alpha^2)} . d\alpha$$
 (14)

$$=\frac{w.\ a.\ P_{max}}{\sqrt{3}}\int_{-\eta}^{\eta}\sqrt{\left(\left(\frac{\sigma_{y}}{P_{max}}\right)^{2}-1+\alpha^{2}\right)}.\ d\alpha.$$
(15)

Using (7) and substituting $P_{max} = \frac{\sigma_y}{\sqrt{1+\theta^2}}$ for dummy variable $\theta > 0$,

$$F_{\rm s} = \frac{2. F_n}{\sqrt{3} \pi} \int_{-\eta}^{\eta} \sqrt{\alpha^2 + \theta^2} \, d\alpha, \tag{16}$$

$$\frac{\sqrt{3}\pi F_{s}}{2F_{n}} = \Big|_{\alpha=-\eta}^{\alpha=\eta} \frac{1}{2}\alpha\sqrt{\alpha^{2}+\theta^{2}} + \frac{\theta^{2}}{2}\ln(\alpha+\sqrt{\alpha^{2}+\theta^{2}})$$
(17)

$$\frac{\sqrt{3}\pi F_{s}}{2F_{n}} = \eta \sqrt{\theta^{2} + \eta^{2}} + \frac{\theta^{2}}{2} \ln \frac{\sqrt{\theta^{2} + \eta^{2}} + \eta}{\sqrt{\theta^{2} + \eta^{2}} - \eta}$$
(18)

$$\frac{F_{\rm s}}{F_{\rm n}} = \frac{2}{\sqrt{3}\pi} \left(\eta \sqrt{\theta^2 + \eta^2} + \frac{\theta^2}{2} \ln \frac{\sqrt{\theta^2 + \eta^2} + \eta}{\sqrt{\theta^2 + \eta^2} - \eta} \right)$$
(19)

To simplify (19), it is assumed that 75% of the contact width has yielded, or η = 0.75. The normal stress goes to zero at the edges of the contact width, and hence the material at that location can be assumed to not have yielded, as discussed in [7]. Expression (19) can be used to compute the yielded area ratio θ as a function of the ratio of shear and weld forces in UAM. This relationship is plotted in Fig. 3. The minimum ratio of the shear and weld forces to yield 75% of the contact width is identified by the X-intercept as 0.2. For a weld force of 5000 N, this corresponds to a minimum shear force of 1000 N.

The value of the maximum normal stress P_{max} can be calculated using the value of θ estimated using (19). The shear stress distribution $\tau(x)$ can then be estimated by substituting this value of P_{max} into (12). This will be useful to estimate the plastic deformation energy E_{pl} as a function of process parameters in Section 2.2.3.

For the example case of $F_n = 5000 \,\mathrm{N}$ and $F_s = 2000 \,\mathrm{N}$ in Fig. 3 when $\theta = 0.7$, The maximum normal pressure P_{max} , normal stress distribution $\sigma(x)$, contact half-width a, and shear stress distribution $\tau(x)$ for this case are computed using (7) and (12) as

$$P_{max} = \frac{\sigma_y}{\sqrt{1 + \theta^2}} = 0.82\sigma_y \tag{20}$$

$$a = \frac{2F_n}{\pi w \sigma_y} \sqrt{1 + \theta^2} = \frac{0.77F_n}{w \sigma_y}$$
 (21)

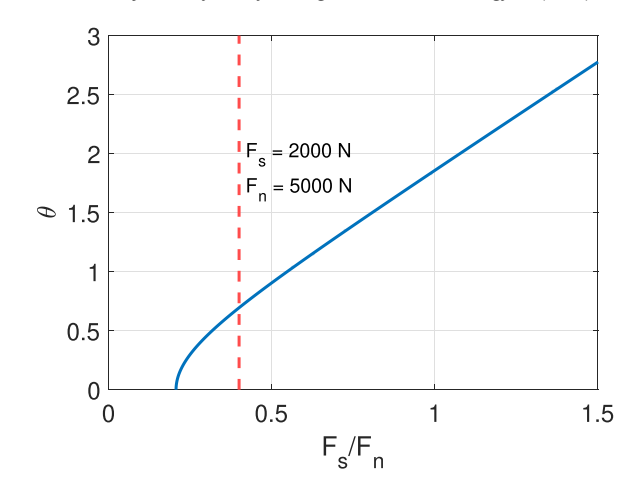


Fig. 3. The normal pressure ratio θ is plotted for different ratios of shear force F_s and weld force F_n using (19). The minimum value of the force ratio is 0.2 when θ = 0. The dotted red line denotes the value of (18) at a weld force F_n = 5000 N and shear force F_s = 2000 N, which are typical parameters used to weld Al 6061-H18 foil, as detailed in [11]. The intersection of the red dotted line and the blue graph is at θ = 0.7.

$$\tau(x) = \frac{1}{\sqrt{3}} \sqrt{\sigma_y^2 - 0.67\sigma_y^2 \left(1 - \left(\frac{x}{a}\right)^2\right)}$$
 (22)

$$= \frac{\sigma_y}{\sqrt{3}} \sqrt{0.33 + 0.67 \left(\frac{x}{a}\right)^2}$$
 (23)

The value of $\tau(x)$ at the end of the contact patch equals one-third of the yield strength as expected since the normal pressures are zero. The maximum normal pressure is always proportional to the material yield strength and the contact half-width is inversely proportional to the material yield strength. The normal and shear stress profiles in the contact width region are plotted for different values of η in Fig. 4(a) and (b), respectively.

Plastic deformation energy estimation

The UAM welder imparts a sinusoidal motion to the top of the foil being welded. Starting at the mean position, the incremental displacement dy leads to an incremental shear plastic strain $d\gamma = d(y - y_{slip})/t_f$ where t_f is the thickness of the foil and dy_{slip} is the incremental frictional slip, as illustrated in Fig. 2(b). It is not expected that asperity-level deformations result in significant differences in the energy of plastic deformation, and are can thus be neglected. Since the elastic component of the strains is also neglected, the incremental plastic strain tensor is given as

$$d\varepsilon_{ij} = \begin{bmatrix} 0 & 0 & 0 \\ 0 & 0 & d\gamma/2 \\ 0 & d\gamma/2 & 0 \end{bmatrix}. \tag{24}$$

The incremental work done for plastic deformation of the weld foil dW_{pl} for an incremental welder displacement dy and incremental slip dy_{slip} between the foils is given by

$$dW_{pl} = \int_{-a}^{a} \frac{1}{2} s_{ij}(x) d\varepsilon_{ij}(x). \ w. \ t_f. \ dx$$
 (25)

$$= \int_{-a}^{a} \tau(x) \frac{dy - dy_{slip}(x)}{t_f} w t_f dx = F_s dy - \int_{-a}^{a} \tau(x) dy_{slip}(x) w dx.$$
 (26)

The rate of plastic work \dot{W}_{pl} can be calculated as

$$\dot{W}_{pl}(t) = \frac{dW_{pl}}{dt} = F_s \cdot \frac{dy}{dt} - \int_{-a}^{a} \tau(x) \frac{dy_{slip}(x)}{dt} dx$$

$$= F_s \dot{\delta}_{welder} - \int_{-a}^{a} \tau(x) \dot{\delta}_{slip}(x) w dx. \tag{27}$$

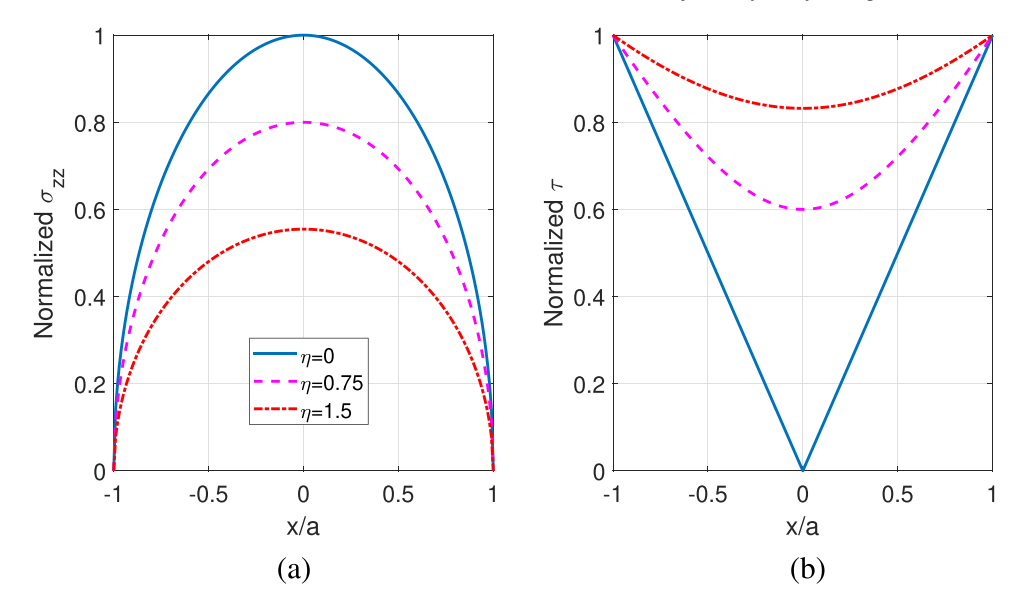


Fig. 4. The normal and shear stresses along the contact width are plotted vs. the X-position normalized by the contact width a: (a) normalized normal stress = $\frac{\sigma(x)}{\sigma_y}$ from (7) and

Assuming that the slip velocity and welder velocity are in phase, the rate of work averaged over one period of oscillation T can be computed as

$$\dot{W}_{pl}^{avg} = \frac{1}{2} F_s |\dot{\delta}_{welder}| - \frac{1}{2} F_s \int_{-a}^{a} \frac{\tau(x)}{F_s} |\dot{\delta}_{slip}(x)| w dx.$$
 (28)

Here, the first term is the rate of total mechanical work done by the welder, defined in the work of [27], and the second term is the portion lost due to slip. The energy of plastic deformation E_{pl} at a single location in the foil is given by the product of the average rate of work and the time spent by the welder over the location:

$$E_{pl} = \dot{W}_{pl}^{avg} \frac{2a}{|\dot{x}|} = \frac{a}{|\dot{x}|} F_s \left(|\dot{\delta}_{welder}| - \int_{-a}^{a} \frac{\tau(x)}{F_s} |\dot{\delta}_{slip}(x)| w dx \right), \tag{29}$$

where $|\dot{x}|$ is the weld speed. For the case of unsuccessful welds, when $|\dot{\hat{s}}_{slip}(x)| = |\dot{\hat{s}}_{welder}|$, the energy of plastic deformation is $E_{pl} = 0$.

Model for frictional dissipation energy

The heat generation due to friction between foils per unit time is given by the following equation:

$$\dot{q}_f(t) = \int_{-a}^a \tau_f(x) \dot{\delta}_{slip}(x) w dx. \tag{30}$$

Here, \dot{q}_f is the rate of heat generation due to friction, a is the half-width of the contact region, $\dot{\delta}_{slip}(x)$ is the slip between the foils at a distance x away from the welder, $\tau_f(x)$ is the frictional stress at that position, and w is the width of the foil. Assuming Coulomb friction and averaging over one period of vibration, (30) simplifies to

$$\dot{q}_f^{avg} = \frac{1}{2} \int_{-a}^a \mu \sigma(x) |\dot{S}_{slip}|(x) w dx, \tag{31}$$

where μ is the Al-Al friction coefficient and $|\dot{\delta}_{slip}|(x)$ is the magnitude of the slip velocity between the foils. In the limiting case, it is assumed that there is pure slip between two foils being welded. This leads to all the deformation of the welder being transformed to frictional slip deformation between the weld foils. Then,

$$\dot{q}_f^{avg} = \frac{1}{2} \int_{-a}^{a} \mu \sigma(x) |\dot{\hat{\sigma}}_{welder}| w dx = \frac{1}{2} \mu F_{N}. |\dot{\hat{\sigma}}_{welder}|,$$
(32)

where $|\dot{\delta}_{welder}|$ is the magnitude of the welder's vibration velocity.

The frictional energy dissipation E_f at a single location in the foil is given by the product of the average rate of work and the time spent by the welder over the location:

$$E_f = \dot{q}_f^{avg} \frac{2a}{|\dot{x}|} = \frac{a}{|\dot{x}|} \int_{-a}^{a} \mu \sigma(x) |\dot{\sigma}_{slip}|(x) w dx, \tag{33}$$

where $|\dot{x}|$ is the weld speed. In the case where there is no plastic deformation in the foil, the friction coefficient μ will take the value of F_s/F_n .

Thermal model

The total heat generation comes from losses in plastic deformation and frictional dissipation. The fraction of plastic energy that is converted to heat, the Taylor-Quinney coefficient, is β and a typical value of 0.9 for aluminum is chosen as used by [25].

During the ultrasonic metal additive manufacturing (UAM) process, heat is generated from two sources: interfacial friction and plastic deformation. The transient temperature field can be estimated using the following equation:

$$\rho c \frac{\partial T}{\partial t} = k \left(\frac{\partial^2 T}{\partial x^2} + \frac{\partial^2 T}{\partial y^2} + \frac{\partial^2 T}{\partial z^2} \right) + q_{total}, \tag{34}$$

$$q_{total} = \beta E_{pl} + E_{f}$$

$$= \frac{a}{|\dot{x}|} \Big(\beta F_{s} |\dot{\delta}_{welder}| - \beta \int_{-a}^{a} \tau(x) |\dot{\delta}_{slip}(x)| w dx + \int_{-a}^{a} \mu \sigma(x) |\dot{\delta}_{slip}|(x) w dx \Big).$$
(35)

Here, $\frac{\partial T}{\partial t}$ is the change in the temperature with respect to time, β is the material Taylor-QUinney coefficient, ρ is the material density, c is the material specific heat, q is the heat generation rate and k is the thermal conductivity. Boundary conditions for convection are shown in (36) and those for heat flux are shown in (37):

$$-k\frac{\partial T}{\partial n} = h(T_a - T_i),\tag{36}$$

$$k\frac{\partial T}{\partial n} = q_b,\tag{37}$$

Table 1Summary of thermal properties used for the transient thermal finite element (FE) analysis using COMSOL.

		Aluminum	AISI 4340
Specific heat capacity	J/(kg.K)	900	475
Density	kg/m³	2700	7850
Thermal conductivity	W/(m.K)	201	44.5

where h is the material surface heat transfer coefficient, n is the normal direction, T_a is the air temperature, T_i is the boundary temperature, and q_b is the boundary heat flux.

Transient thermal finite element model

A transient thermal simulation of the rotating welder and the translating workpiece are simulated using COMSOL. Properties of the materials used are listed in Table 1. The welder rotates such that there is no rolling slip with respect to the workpiece. The weld foils and the baseplate are modeled as one piece since they are all made of aluminum alloys. A pairwise thermal contact is defined between the welder and the workpiece, with heat generation. Thermal resistance due to asperities is neglected since sufficient weld force is present in UAM to collapse the asperities in the foil. The workpiece and the foil being welded are modeled as a single block, similar to the work of [25].

A rotating-domain deforming geometry is used to rotate the welder at a constant angular velocity. A prescribed deforming geometry is used to translate the workpiece at the weld speed. A pairwise thermal contact is defined between the steel welder and the aluminum workpiece. AISI 4340 is used for the steel material properties for the welder and aluminum 6063-T83 is used for the workpiece's material properties Fig. 5.

The combined heat generated due to friction and plastic deformation (q_{total}) is partitioned at the contact interface in accordance with the Charron's relationship, detailed in [33], where the generated heat is partitioned into rq_{total} into the steel welder and (1-r) q_{total} to the foils. The expression for r is

$$r = \frac{1}{1+\xi}$$
, where $\xi = \sqrt{\frac{\rho_1 C_{p,1} k_1}{\rho_2 C_{p,2} k_2}}$. (38)

Here, ρ_1 , $C_{p,1}$, and k_1 are the density, specific heat capacity, and thermal conductivity of the foil, and similarly with subscript 2 for

the steel welder. For welding aluminum, 16.5% of the heat generated is lost to heating the steel welder. It is assumed that the heat generated due to plastic deformation can be approximated to be at the horn-foil interface due to the small thickness of the feedstock.

The transient simulation is run with a sample heat generation of 2000 W at the welder-foil interface in Fig. 6, which results in a predicted temperature increase of 107 K for a weld speed of 84.67 mm/s (200 in/min). The thermal FE problem solved is linear, and thus, the temperature increase measured using the IR camera system can be used to calculate the actual heat generation Q_{UAM} for a given set of process parameters, as illustrated in Fig. 1. Simulations show that the peak temperature is not sensitive to the convection coefficient between the welder and air, and hence a typical surface-to-air value of $20 \, \text{W/m}^2$. K is used.

Parametric study using FE model - effect of weld speed

A simple analytical moving heat source model for heat generation in UAM like the one used by [28] does not account for the rotation of the welder. The welder rolls without slip over the foil during the UAM process. The effect of weld speed on weld temperature is estimated using the FE model by varying the weld speed between 125, 200, and 275 in/min and plotting the FE estimates of peak welder temperature in Fig. 7(a). The results show that the peak temperature values reach a steady value after about 0.5 s and the steady peak temperature increases with decreasing weld speed. The slight oscillation seen in the temperature is due to the size of the mesh elements used. Reducing the mesh size from the chosen value did not affect the peak temperatures estimated.

The actual temperature profile of the welder surface is shown in Fig. 7 (b), (c), and (d) for 52.92 mm/s (125 in/min), 84.67 mm/s (200 in/min), and 116.4 mm/s (275 in/min), respectively. The profiles show a peak temperature at the welder contact point, and high temperature gradients as a function of angle.

IR experiments and data analysis

The in-situ temperature distribution during welding is measured using a non-contact (IR) longwave infrared camera (FLIR A6751sc). A frame rate of 30 Hz is used and the response time for the IR camera to identify a temperature change is 190 μ s. The spectral range chosen for the temperature range of interest is 7.5–11 μ m. The sensor in the

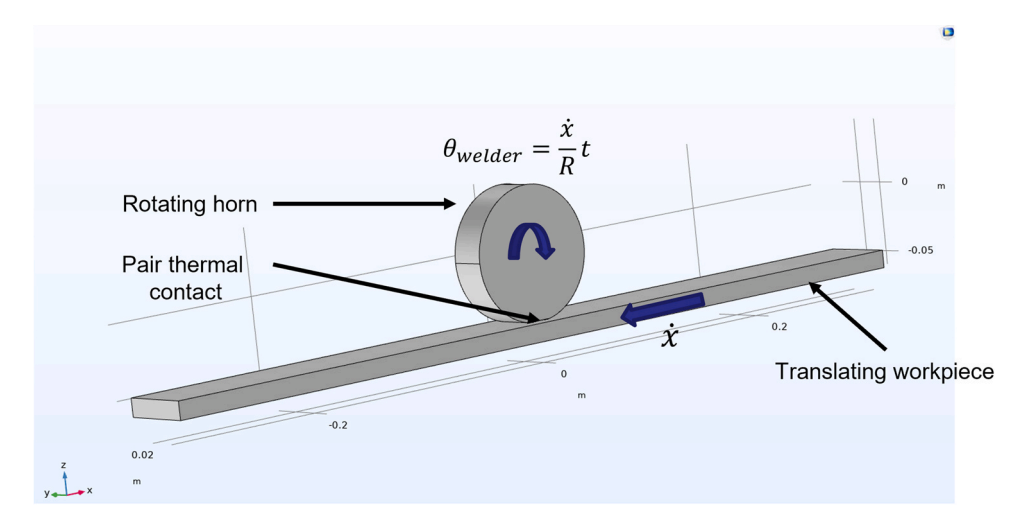


Fig. 5. Transient thermal simulation of the rotating welder and the translating workpiece simulated using COMSOL. Note that the 20 kHz vibration of the welder is the Y-direction. The welder rotates such that there is no rolling slip with respect to the workpiece. The weld foils and the baseplate are modeled as one piece since they are all made of aluminum alloys. A pairwise thermal contact is defined between the welder and the workpiece, with heat generation at the interface.

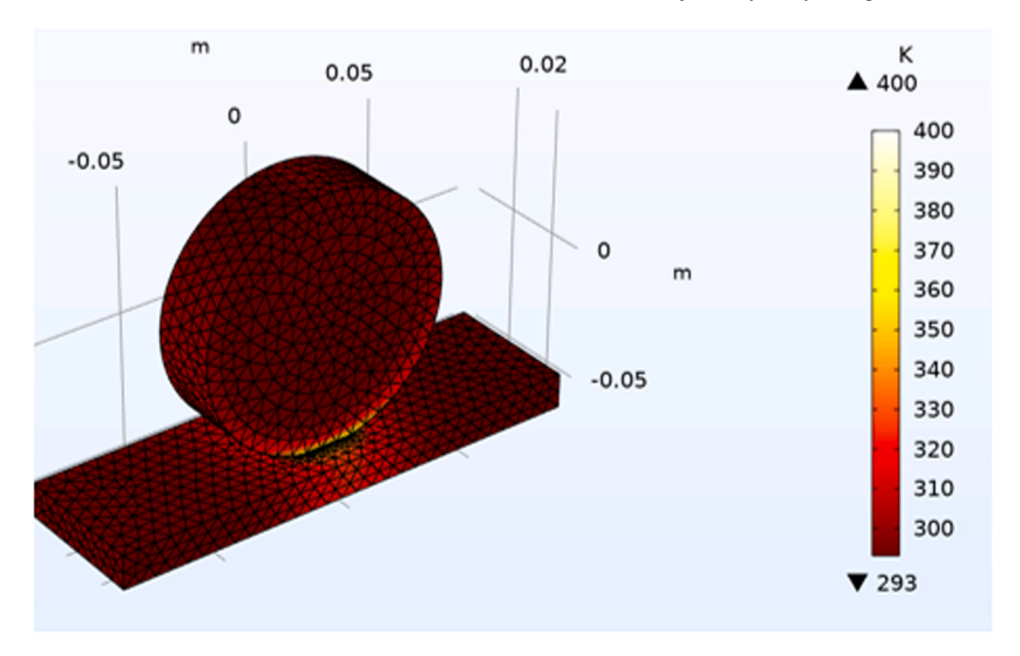


Fig. 6. Temperature field in K under a rotating welder and a feedstock translating at a speed of 84.67 mm/s (200 in/min) simulated using COMSOL. Thermal power of 2000 W is input to the welder-workpiece interface which is partitioned based on Charron's rule (38). A temperature increase of 107 K from ambient is estimated.

camera converts the incoming infrared photons into a 640×480 voltage map using the emissivity of the welder surface, which was measured to be 0.9 in a calibration experiment using a K-type thermocouple, detailed in Section 3.4. The camera is mounted on a boom arm as shown in Fig. 8. A standard ruler is used to calibrate the pixel-to-pixel distance at the standoff distance used. A total of 13 pixels are required for 1 mm marking on the ruler, which translates to a pixel size of 76 μ m, which is about half the thickness t_f of the UAM foil.

Calibration of infrared emissivity of the welder surface

Al 5052-H38 foil that is 0.152 mm thick and 25.4 mm wide is fed using the tape feeder and tensioned using a force of 90 N around the welder. An OMEGA Type K AWG 40 thermocouple (0.080 mm tip diameter) is bonded to the side of the steel welder using superglue to measure the temperature at the interface of the steel welder, shown in Fig. 9(a). Fig. 9(a) also shows the exposed portion of the welder where the infrared measurements are made. This is possible since the welder is 10% wider than the foil. The transducers are excited at a vibration amplitude of 26 μm to generate heat through sliding friction between the vibrating welder and the aluminum foil. The foil surface does not reflect its true temperature to the infrared camera since the emissivity of aluminum foil is too low (< 0.1). The emissivity value of the steel surface is varied until good agreement (within 3 K) is achieved between the infrared and thermocouple temperature estimates. The small differences are attributed to the effect of the superglue on the time constant of the thermocouple and the small distance between the location of the thermocouple and the surface seen by the camera. An emissivity value of 0.9 is chosen for the steel welder.

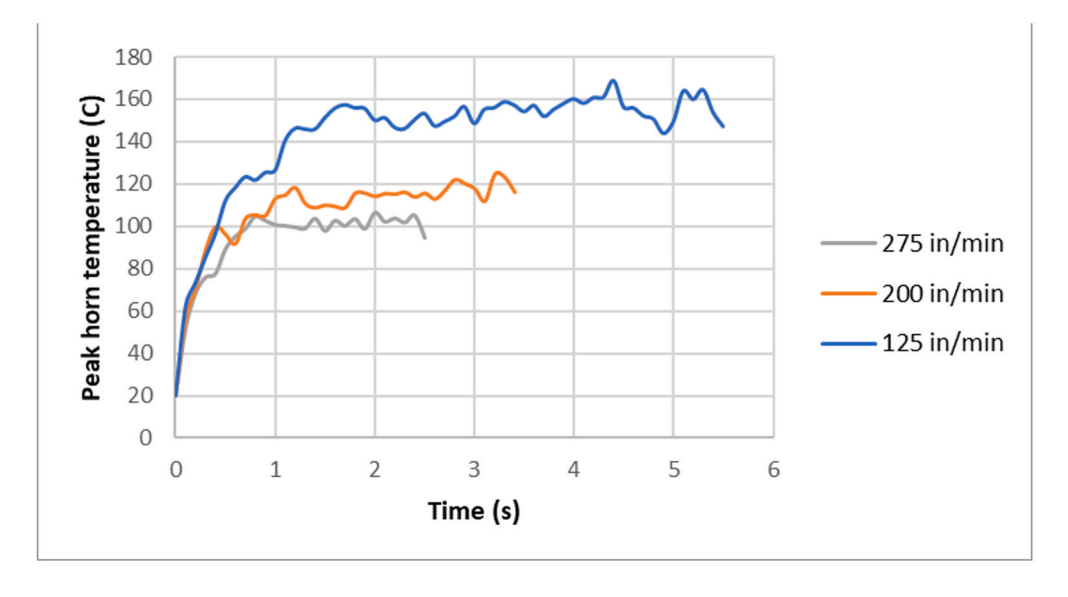
Model validation

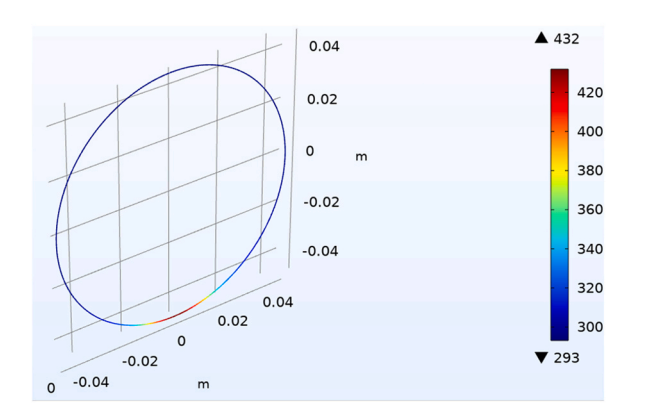
Al 6061-O, 6061-H18, 5052-O, and 5052-H38 feedstock are welded onto a 12.7 mm (0.5 in.) thick Al 6061-T6 baseplate. The temperature is found to be similar for the first foil to baseplate weld and the first foil to second foil welds. Representative IR

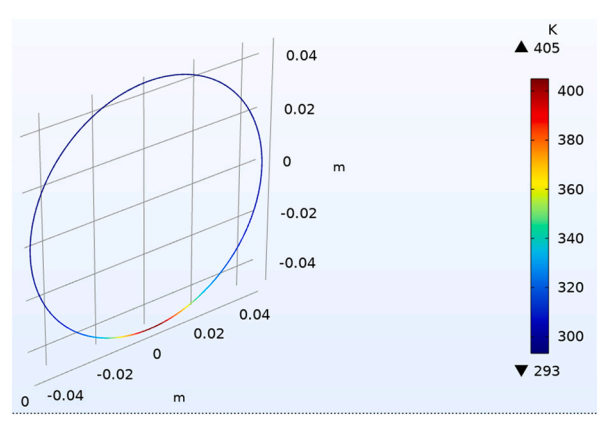
images for Al 5052-H38 and Al 6061-O foils are shown in Fig. 10(b) and (d), respectively. Three key features are observed in these IR images: (i) the machined Al 6061-T6 baseplate acts as a perfect mirror creating a mirror image of the welder infrared image; (ii) the peak temperature on the welder is reached at the welder-foil interface and is uniform along the width of the foil interface; and (iii) the peak temperature of the welder is steady during the welding process, as seen in Fig. 10(a) and (c). Note that the temperature at the weld interface is expected to be close to the value at the horn-foil interface due to the small thickness of the foil. The peak temperature is estimated as the time-average of the measured maximum temperature from the infrared video during welding. The temperature increase for Al 6061-O foil is 88 K (peak temperature is 118°C), while the temperature increase for Al 5052-H38 is 44 K (peak temperature is 74° C). This difference is attributed to the potential difference in the Taylor-Quinney coefficient between 5000-series and 6000-series aluminum alloys. This peak value is used for validation against the peak temperature from the transient thermal FE model.

Temperature-dependent mechanical properties for Al 6061-O, Al 5052-O, and Al 5052-H38 are obtained from the ASM materials handbook [1]. Properties for Al 6061-H18 are experimentally obtained from uniaxial tensile testing measurements in a temperature-controlled chamber. The yield strength of all the foils reduces by less than 10% up to 120°C, which is the maximum measured weld temperature for the range of weld parameters used. Hence, the effect of thermal softening on the yield strength of the foils is neglected in the analytical model. If the material being welded exhibits significant thermal softening during UAM, the weld temperature needs to be iterated over a range of possible values until the estimate of heat generation from the structural model with thermal softening matches that from the thermal model.

The experimentally obtained weld temperatures from infrared imaging and the corresponding temperature estimate from the analytical model are shown in Fig. 11. The model with β = 0.9 underestimates the temperature increase for Al 6061-0, and this is because the model does account for work hardening (cold working) of the material and elongation in the rolling direction during UAM,







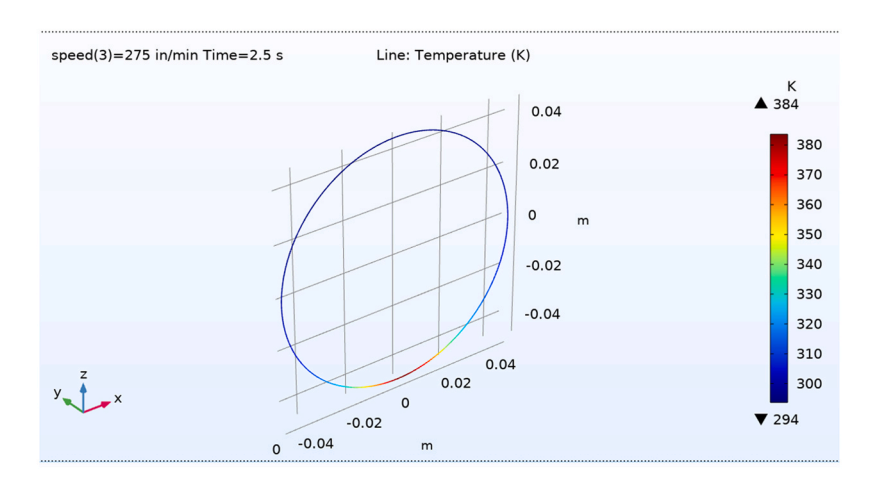


Fig. 7. Temperature field in K under a rotating welder with a translating feedstock simulated using COMSOL at different weld speeds, and the corresponding temperature profile on the welder for a 2000 W reference heat input at the welder-workpiece interface: (a) temperature at the foil-welder interface as a function of time from the FE model. The temperature reaches a steady value which corresponds to the weld temperature measured by the IR camera in Section 3.3; temperature vs. angle plots of the welder for weld speed \dot{x} of (b) 52.92 mm/s (125 in/min), (c) 84.67 mm/s (200 in/min), and (d) 116.4 mm/s (275 in/min).

which is significant for a soft material like Al 6061-O. For the 5052 series aluminum, a choice of β =0.6 is a better fit for the weld temperatures for Al 5052-H38. This model also over-estimates the temperature increase for the 5052-O alloy as work hardening was not incorporated.

Process-property relationships for UAM of aluminum

A simple empirical model for the shear strength $\tau_{s,weld}$ of the weld interface is developed similar to the model by [30] for cold roll bonding. The shear strength of the bulk material $(\tau_{s,bulk})$ is used to

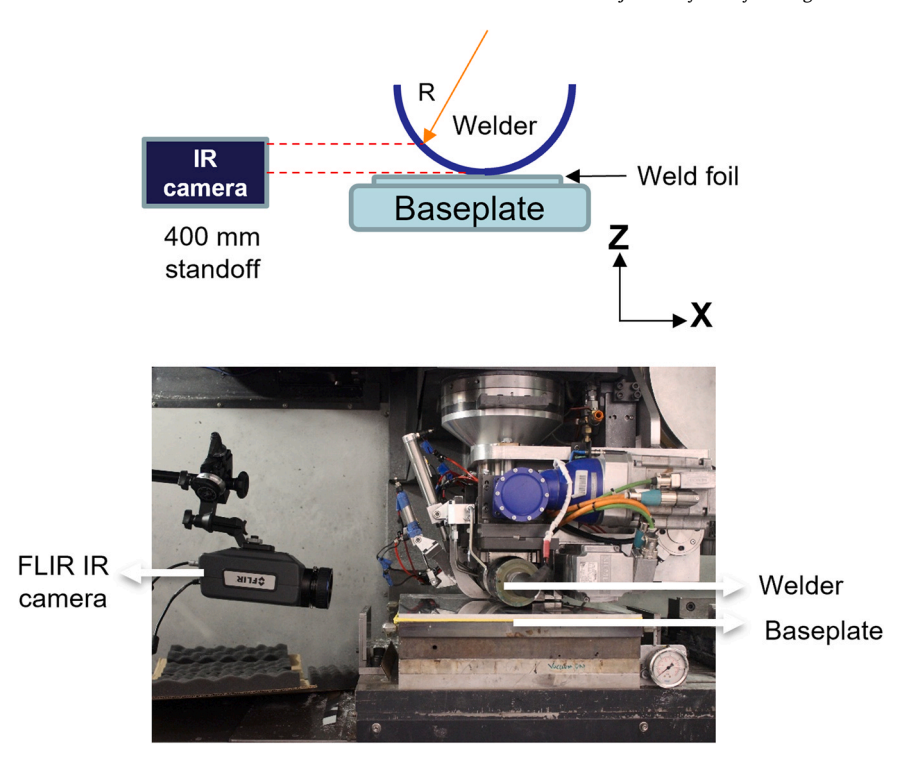


Fig. 8. Setup to measure the weld temperature during UAM: (a) illustration of the IR camera positioned to view the front of the welder during welding; (b) image of the FLIR A6751sc camera positioned using a Manfrotto boom arm.

normalize the weld strength. The model is modified to use the energy of plastic deformation per unit length E_{pl} instead of the thickness reduction:

$$\frac{\tau_{s,weld}}{\tau_{s,bulk}} = H \left(1 - \frac{(1 - E_{pl}/A)^2}{(1 - E_{pl}^{th}/A)^2} \right), \tag{39}$$

where H is an empirical hardening coefficient, Epl^{th} is the threshold energy of plastic deformation for bond formation, and A is a coefficient used to normalize the energy of plastic deformation. The coefficient H accounts for the effect of work-hardening to improve the strength of the foil material. The value of H is set as 1 for Al 6061-H18 since the temper is fully cold-worked. The model coefficient A is chosen by fitting the model against the strength measurements for Al 6061-H18 to be 30 kJ/m. This calibrated model is then used to determine the value of H for Al 5051-O is determined by fitting the model against strength measurements for Al 5052-O. The value for a good fit is H = 2.5. This calibrated model can be used to determine the weld strength for the UAM of aluminum and other metals. The

model is compared against experiments in Fig. 12 and found to be in good agreement.

Energy flow map for UAM of aluminum

A comprehensive map of all the energies involved in the UAM process is shown in Fig. 13. The input electrical energy to the transducers, E_{ip} , is converted into mechanical work at the welder-foil interface utilizing an efficiency of about 87.5% as computed by [11]. The rate of energy required to disperse the oxide layer for aluminum is estimated as follows. The thickness of an aluminum oxide film at room temperature has been measured by [15] to be on the order of nanometers. The energy required to crack the oxide layer is thus expected to be negligible in UAM when compared to the input energy. Venkatraman et al. [26] showed that the energy stored in the interface microstructure, estimated using the Read-Shockley relationship, is also negligible when compared to the input energy. The remaining mechanical energy is converted predominantly into the

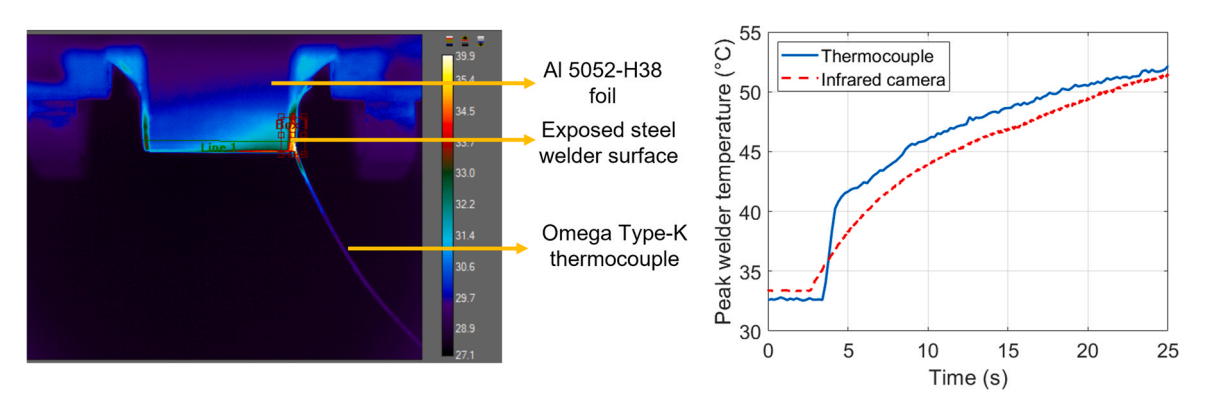


Fig. 9. Calibration of the infrared emissivity of the steel welder using an OMEGA Type K AWG 40 thermocouple (0.080 mm tip diameter): (a) infrared image of the setup showing the thermocouple bonded to the side of the welder and the infrared camera estimating the welder temperature from the exposed surface of the steel welder (enclosed in the red rectangle); (b) comparison of the measured temperatures estimated using the thermocouple and infrared measurements.

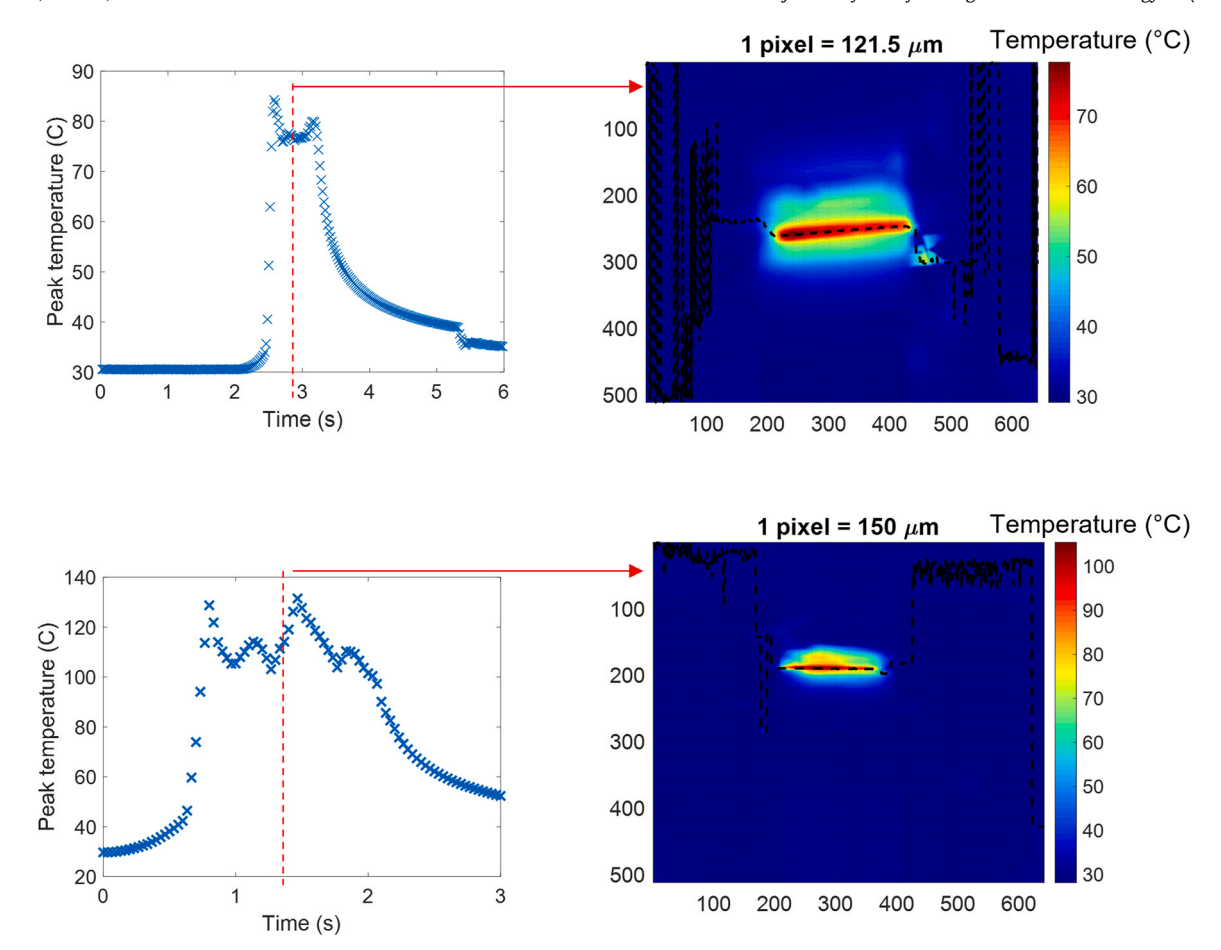


Fig. 10. IR temperature measurements during the UAM of Al foils onto a 0.5 in thick Al 6061-T6 baseplate using a weld amplitude of $32 \mu m$, weld force of 5000 N and a weld speed of 84.67 mm/s (200 in/min): (a) peak temperature vs. time for Al 5052-H38, with a steady weld temperature of 74° C; (b) infrared image during welding of Al 5052-H38, where the black dotted line follows the point with maximum temperature from left to right; (c) peak temperature vs. time for Al 6061-O, with a steady weld temperature of 118° C; (d) infrared image during welding of Al 6061-O, where the black dotted line follows the point with maximum temperature from left to right.

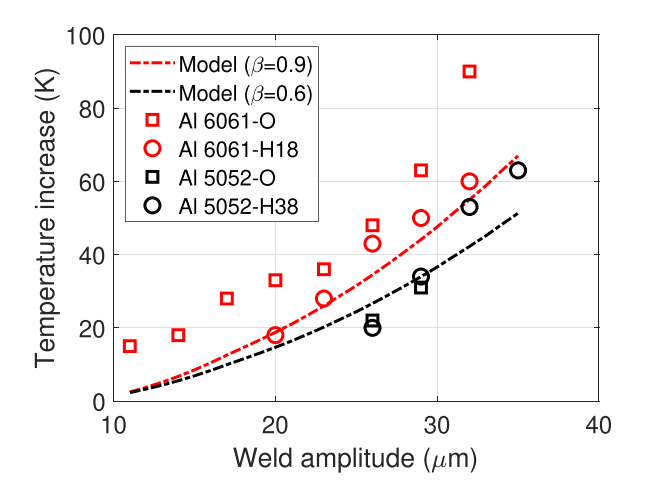


Fig. 11. Weld temperatures for Al 6061-O, Al 6061-H18, Al 5052-O, and Al 5052-H38 measured using infrared imaging using a weld force of 5000 N and a weld speed of 84.67 mm/s (200 in/min) and varying weld amplitude. The measurements are compared against estimates from the analytical model shown using dotted lines. The total heat generated is estimated using (35) and input to the thermal finite element model to predict the temperature increase. Two possible values of the parameter β are chosen to account for the differences between the alloys. The annealed tempers have a higher mismatch with the model since work hardening is accounted for in the model, which under-predicts the plastic deformation energy.

two key energies involved in the process: plastic deformation and frictional slip. The rest is assumed to be used to collapse the asperities on the surface of the two foils being welded. About 90% of the plastic deformation energy is assumed to be converted to heat (β = 0.9), and the frictional dissipation is completely converted to heat. About 16.5% of the generated heat is conducted to the steel welder, and the remaining 83.5% increases the temperature of the foil and workpiece.

Rusinek and Klepaczko [20] showed that about 10% of the plastic deformation energy is used for the creation, rearrangement of crystal defects, and the formation of dislocation structures. It is expected from the dislocation density-based crystal plasticity model developed by [18] that the geometrically-necessary dislocation (GND) density increases with each cycle of vibration from the welder, which is a means to store the energy of plastic deformation. The work found that a GND density of $6 \times 10^{15} \, \mathrm{m}^{-2}$ is expected after 3000 cycles of deformation for UAM of Al 3003-H18. The statistically-stored dislocation density is much smaller than the geometrically-necessary dislocation density, and as such it can be neglected. This dislocation density determines the sub-grain diameter in the resulting microstructure.

A figure of merit can defined for the UAM process from the energy flow map as the fraction of input electrical energy that is used for bond formation. Plastic deformation is the key driver of solid-state bond formation, and hence $1-\beta$, or 10% of the plastic

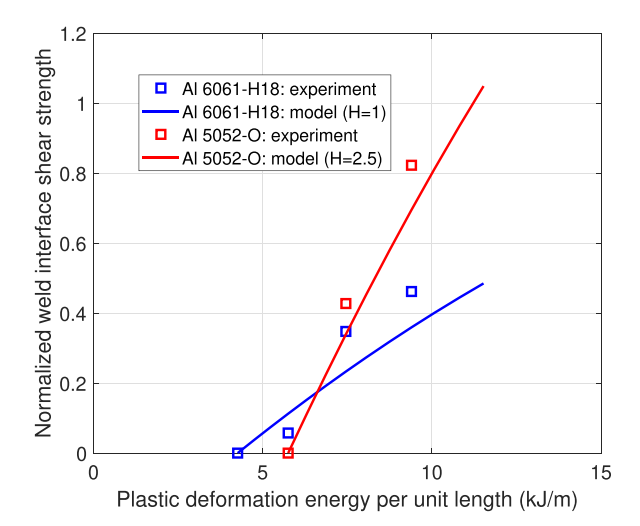


Fig. 12. The shear strength of Al 6061-H18 and Al 5052-O foil-foil welds normalized by the bulk shear strength of the foil material is plotted against the plastic deformation energy per unit length of the weld. The samples tested were welded using a weld force of 5000 N and a weld speed of 84.67 mm/s (200 in/min). The weld amplitude is varied between 23 and 32 μ m to fabricate the welds. The expression in (39) is used to estimate the normalized weld interface shear strength. The higher increase in shear strength for Al 5052-O material is attributed to work hardening, and an empirical hardening coefficient of 2.5 is used to account for this.

deformation energy is used directly for bond formation. In addition, part of the heat generated also lowers the yield stress of the foil material, reducing the weldability threshold E_{pl}^{th} from (39). This reduction is characterized by the relationship between the flow stress (or yield stress) and temperature which [3] showed to fit a power

law relationship for most aluminum alloys. The useful energy is thus the portion of heat generation that is not lost via conduction to the welder. The useful energy E_{useful} and the figure of merit α are thus defined as

$$E_{useful} = (1 - \beta)E_{pl} + 0.83q_{total},$$
 (40)

$$\alpha = \frac{E_{useful}}{E_{ip}}. (41)$$

The figure of merit for the case described in Fig. 13 is computed to be 69.4%. This value is lower than the efficiency of the welding assembly, which is close to 85%.

The figure of merit α in (41) is dependent on the following factors: (i) the thermal properties of the foil and horn which determine the heat partition coefficient at the interface; (ii) Taylor-Quinney coefficient β of the foil material; (iii) success of weld formation which determines the partition between plastic deformation and frictional slip; (iv) foil and workpiece geometry. Each of these factors can be adjusted to improve the figure of merit of UAM. Han et al. [10] have shown that the modification of the horn surface with a surface coating to improve thermal insulation can increase the weld temperature and also the resulting mechanical strength of as-welded parts for the UAM of 4130 carbon steel.

Conclusions

A model for the flow of energy in ultrasonic additive manufacturing of aluminum was developed by quantifying the different energies involved in the UAM process. To guide model development, the UAM of annealed and fully work-hardened tempers of 6061 and 5052 aluminum alloys was investigated. Infrared thermography was used to measure in-situ weld temperature as a function of vibration amplitude and weld speed. A temperature increase of up to 100 K

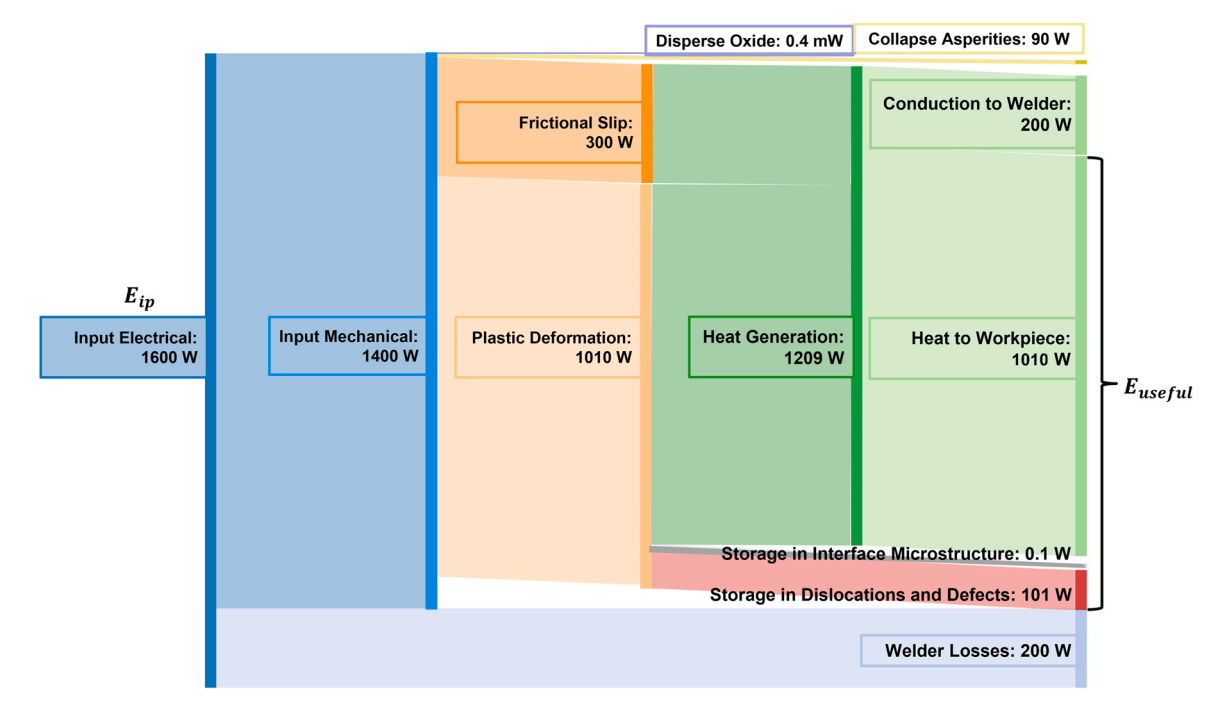


Fig. 13. Flow of electrical energy per unit time (E_{ip}) from the welder (electrical) to the different energies involved in the UAM process. A energies were estimated using the following weld parameters for the UAM of Al 6061-H18: weld amplitude of 32 μ m, weld speed of 84.67 mm/s (200 in/min), and a weld force of 5000 N. The useful energy E_{useful} for bond formation is defined in (40).

was observed for the UAM of Al foils at weld amplitudes between 11 and 35 μ m. A transient thermal FE model for heat transfer was developed and validated using the infrared temperature measurements. The validated model is able to estimate the relative fraction of heat generation from plastic deformation and friction, enabling the estimation of weld temperature. This model is useful for the embedding of sensitive sensors and materials using UAM, since the process parameters can be chosen such that the weld temperature stays below the critical or highest safe temperature of the sensitive material to avoid thermal degradation.

The strength of the weld interfaces was quantified utilizing a shear tester. Weld strengths of up to 50% of the bulk foil shear strength were measured for the UAM of Al 6061-H18 and up to 80% for the UAM of Al 5052-O. The stronger dependence of weld strength on weld amplitude for Al 5052-O is attributed to the work hardening of the annealed foil during the cyclic plastic deformation in UAM, which is absent for the fully-hardened Al 6061-H18. An empirical relationship between the energy of plastic deformation as a function of weld parameters and weld strength was established using expressions from the cold roll bonding literature. The expression accounts for the strength increase with a hardening coefficient and the calibrated model can be used to predict the strength of UAM Al as a function of process parameters.

The flow of energy in the UAM of aluminum was mapped, and the different energies involved in the UAM process were quantified. The formulation was used to develop a figure of merit to qualify the proportion of input energy that is used for bond formation, which was computed to be 69.4% for the process conditions chosen. This figure of merit can be used as a design criterion for an improved use of the input electrical energy for bond formation in UAM, reducing wasted forms of energy such as conduction to the welder or losses in the piezoelectric transducers.

Declaration of Competing Interest

The authors declare the following financial interests/personal relationships which may be considered as potential competing interests: Marcelo Dapino reports financial support was provided by National Science Foundation.

Acknowledgements

Financial support was supplied by the member organizations of the Smart Vehicle Concepts Center (www.SmartVehicleCenter.org), a Phase III National Science Foundation Industry-University Cooperative Research Center under Grant NSF IIP 1738723. Support for U.S. and X.L. was supplied by the National Science Foundation under Grant CMMI/AM 1853632.

References

- ASM Handbook Committee. Properties and Selection: Nonferrous Alloys and Special-purpose Materials. ASM Handbook. Vol. 2. ASM International, Materials Park, OH.
- [2] Bhushan, B., 2013, Contact Between Solid Surfaces. Introduction to Tribology. John Wiley and Sons Ltd, West Sussex, United Kingdom.
- [3] Chamanfar, A., Alamoudi, M.T., Nanninga, N.E., Misiolek, W.Z., 2019, Analysis of Flow Stress and Microstructure During Hot Compression of 6099 Aluminum Alloy (AA6099). Materials Science and Engineering: A, 743:684–696.
- [4] Cheng, X., Li, X., 2007, Investigation of Heat Generation in Ultrasonic Metal Welding Using Micro Sensor Arrays. Journal of Micromechanics and Microengineering, 17/2: 273.
- [5] Cooper, D.R., Allwood, J.M., 2014, The Influence of Deformation Conditions in Solid-state Aluminium Welding Processes on the Resulting Weld Strength. Journal of Materials Processing Technology, 214/11: 2576–2592.
- [6] De Vries, E., 2004, Mechanics and Mechanisms of Ultrasonic Metal Welding. The Ohio State University.

- [7] Foster, D.R., 2014, Mechanical and Thermal Characterization of Ultrasonic Additive Manufacturing. The Ohio State University.
- [8] Fujii, H.T., Shimizu, S., Sato, Y.S., Kokawa, H., 2017, High-strain-rate Deformation in Ultrasonic Additive Manufacturing. Scripta Materialia, 135:125–129.
- [9] Gunduz, I.E., Ando, T., Shattuck, E., Wong, P.Y., Doumanidis, C.C., 2005, Enhanced Diffusion and Phase Transformations During Ultrasonic Welding of Zinc and Aluminum. Scripta Materialia, 52/9: 939–943.
- [10] Han, T., Kuo, C., Sridharan, N., Headings, L.M., Babu, S.S., Dapino, M.J., 2020, Effect of Weld Power and Interfacial Temperature on Mechanical Strength and Microstructure of Carbon Steel 4130 Fabricated by Ultrasonic Additive Manufacturing. Manufacturing Letters, 25:64–69.
- [11] Hehr, A., Dapino, M.J., 2017, Dynamics of Ultrasonic Additive Manufacturing. Ultrasonics, 73:49–66.
- [12] Huang, H., Chen, J., Lim, Y.C., Hu, X., Cheng, J., Feng, Z., Sun, X., 2019, Heat Generation and Deformation in Ultrasonic Welding of Magnesium Alloy AZ31. Journal of Materials Processing Technology, 272:125–136.
- [13] Kelly, G.S., Just Jr, M.S., Advani, S.G., Gillespie Jr, J.W., 2014, Energy and Bond Strength Development During Ultrasonic Consolidation. Journal of Materials Processing Technology, 214/8: 1665–1672.
- [14] Khan, M.A., Madsen, N.H., Chin, B.A., 1984, Infrared Thermography as a Control Tor the Welding Process. Thermosense VI: Thermal Infrared Sensing for Diagnostics and Control, 0446:154–163.
- [15] Le, H.R., Sutcliffe, M.P.F., Wang, P.Z., Burstein, G., 2004, Surface Oxide Fracture in Cold Aluminium Rolling. Acta Materialia, 52/4: 911–920.
- [16] Mohamed, H.A., Washburn, J., 1975, Mechanism of Solid State Pressure Welding. AWS Welding Journal.
- [17] Obielodan, J.O., Ceylan, A., Murr, L.E., Stucker, B.E., 2010, Multi-material Bonding in Ultrasonic Consolidation. Rapid Prototyping Journal, 16/3: 180–188.
- [18] Pal, D., Stucker, B., 2013, A Study of Subgrain Formation in Al 3003H-18 Foils Undergoing Ultrasonic Additive Manufacturing Using a Dislocation Density Based Crystal Plasticity Finite Element Framework. Journal of Applied Physics, 113/20:203517.
- [19] Purwanto, A., Wisnuwijaya, R.I., Sari, E.K., Dwandaru, W.S.B., 2020, Non-contact Temperature Measurement Based on Wienas Displacement Law Using a Single Webcam in the Infrared Spectrum Region. Physics Education, 55/2:025017.
- [20] Rusinek, A., Klepaczko, J.R., 2009, Experiments on Heat Generated During Plastic Deformation and Stored Energy for Trip Steels. Materials & Design, 30/1: 35–48.
- [21] Schick, D., Babu, S.S., Foster, D.R., Dapino, M.J., Short, M., Lippold, J.C., 2011, Transient Thermal Response in Ultrasonic Additive Manufacturing of Aluminum 3003. Rapid Prototyping Journal, 17/5: 369–379.
- [22] Seidt, J.D., Gilat, A., 2013, Plastic Deformation of 2024-T351 Aluminum Plate Over a Wide Range of Loading Conditions. International Journal of Solids and Structures, 50/10: 1781–1790.
- [23] Siggard, E.J., 2007, Investigative Research Into the Structural Embedding of Electrical and Mechanical Systems Using Ultrasonic Consolidation (UC). Utah State University.
- [24] Speka, M., Matteï, S., Pilloz, M., Ilie, M., 2008, The Infrared Thermography Control of the Laser Welding of Amorphous Polymers. NDT and E International, 41/3: 178–183
- [25] Sriraman, M.R., Gonser, M., Fujii, H.T., Babu, S.S., Bloss, M., 2011, Thermal Transients During Processing of Materials by Very High Power Ultrasonic Additive Manufacturing. Journal of Materials Processing Technology, 211/10: 1650–1657.
- [26] Venkatraman, G., Hehr, A., Headings, L.M., Dapino, M.J., 2022, Effect of Process Parameters on the Microstructure of Aluminum Alloys Made Via Ultrasonic Additive Manufacturing. Rapid Prototyping Journal, 27/9: 1650–1663.
- [27] Venkatraman, G., Hehr, A., Headings, L.M., Dapino, M.J., 2021, Effect of System Compliance on Weld Power in Ultrasonic Additive Manufacturing, Rapid Prototyping Journal, 27/9: 1650–1663.
- [28] Ward, A.A., Zhang, Y., Cordero, Z.C., 2018, Junction Growth in Ultrasonic Spot Welding and Ultrasonic Additive Manufacturing, Acta Materialia, 158:393–406.
- [29] Wolcott, P.W., Dapino, M.J., 2017, Ultrasonic Additive Manufacturing. Additive Manufacturing Handbook: Product Development for the Defense Industry. CRC Press/Taylor and Francis, Boca Raton, FL.
- [30] Wright, P.K., Snow, D.A., Tay, C.K., 1978, Interfacial Conditions and Bond Strength in Cold Pressure Welding by Rolling. Metals Technology, 5/1: 24–31.
- [31] Yadav, S., Doumanidis, C., 2005, Thermomechanical Analysis of an Ultrasonic Rapid Manufacturing (URM) System. Journal of Manufacturing Processes, 7/2: 153–161.
- [32] Yang, Y., Ram, G.J., Stucker, B., 2009, Bond Formation and Fiber Embedment During Ultrasonic Consolidation. Journal of Materials Processing Technology, 209/10: 4915–4924.
- [33] Yevtushenko, A., Grzes, P., 2011, Finite Element Analysis of Heat Partition in a Pad/disc Brake System. Numerical Heat Transfer, Part A: Applications, 59/7: 521-542
- [34] Yi, D., Zhang, S., Zhang, H., Zheng, L., Norfolk, M., 2017, Power Consumption and Friction Coefficient in the Ultrasonic Consolidation of Aluminium Alloys. Materials Science and Technology, 33/6: 744–750.
- [35] Zhang, S., Yi, D., Zhang, H., Zheng, L., Zhang, Y., Yang, Z., Norfolk, M., 2015, Towards Understanding of Ultrasonic Consolidation Process with "Process Map. Rapid Prototyping Journal, 21/4: 461–468.